Synchronverter-based frequency control technique applied in wind energy conversion systems based on the doubly-fed induction generator

José Dickson Araújo de Oliveira [a], Francisco Kleber de Araújo Lima [a,*], Fernando Lessa Tofoli [b], Carlos Gustavo Castelo Branco [a]

[a] Federal University of Ceará, Department of Electrical Engineering, Fortaleza, Ceará, Brazil
[b] Federal University of São João del-Rei, Department of Electrical Engineering, São João del-Rei, Minas Gerais, Brazil

ARTICLE INFO

ABSTRACT

The increasing penetration of wind energy conversion systems (WECSs) based on the doubly-fed induction generator (DFIG) has raised serious concerns about the stability of modern power systems. One important issue is the frequency control of interconnected networks, which may become more complex owing to the low inertia of wind turbines. In this context, this work presents a novel frequency control approach that associates the grid-side converter (GSC) with a synchronverter. To assess the performance of the proposed solution, a thorough comparison with other well-known frequency control techniques is presented, that is, pitch angle control and switching angle controller (SAC). Simulation tests of the IEEE 14-bus modified test system are carried out in PSCAD/EMTDC® software to assess the behavior of a 165 MW wind farm (WF) when frequency variations occur. The results show that the classical control approaches can restore the system frequency within a time interval up to 63% shorter and a frequency dip lower than 13% when compared with WECSs that cannot provide frequency support. In turn, the synchronverter-based technique presents improved performance while attenuating a frequency dip by 45.7% and 56.9% when compared with the aforementioned strategies and WECSs without frequency support, respectively.

1. Introduction

Wind energy conversion systems (WECSs) have emerged as an interesting solution for diversifying the energy matrix of several countries worldwide owing to the intrinsic renewable and abundant nature of the wind [1]. In this context, advances in wind turbine and generator technology caused a significant reduction in energy costs associated with wind farms (WFs) over the last years [2]. However, the high penetration of WFs may affect the power system stability significantly. It is also worth mentioning that the frequency variation of power systems due to fluctuations in the wind generator output increases, causing changes in the operation point of turbines. Even though WFs are provided with a frequency relay responsible for disconnecting them after a given frequency disturbance, the massive disconnection of generating units may lead to power oscillations [3].

Thus, modern grid codes have imposed several restrictions for the connection of WFs to the grid considering both steady-state and transient conditions, while incorporating the capacity of providing frequency control, active and reactive power flow control, and voltage ride through as ancillary services [4]. Variable-speed wind turbines (VSWTs) employing the permanent magnet synchronous energy generator (PMSG) and the doubly-fed induction generator (DFIG) associated with a power electronic interface can be used for this purpose [5]. Among them, DFIG-based WECSs are the most popular choices because the back-to-back converter processes only a small portion of the rated power, whereas one can easily control the active power and reactive power flow [6]. Unfortunately, VSWTs are immune to the grid frequency variation, causing severe stability issues in conventional power systems based on synchronous generators [7]. The insensitivity of DFIGs to the frequency deviation is due to the rotor connected to the grid through an ac-dc-ac converter, thus decoupling the active power output and the grid frequency. This aspect also prevents the frequency variation damping through the supply or absorption of kinetic energy. Another important issue is that DFIGs typically operate in maximum power point tracking (MPPT) mode, limiting the power reservation and the capacity to increase the power output when necessary [8].

Frequency control has been thoroughly addressed in the literature in terms of distinct solutions, whereas a comprehensive review of the existing solutions is presented in [9]. An attempt to quantify the short-term active power support is addressed in [10] and, according to [11], there are two major approaches for this purpose. One can achieve primary frequency control by the de-loading operation of VSWTs to reserve the active power output instead of performing MPPT. On the other hand, virtual inertia control allows emulating the behavior of synchronous generators in frequency excursion events [12].

Considering the limited power reservation capacity of the aforementioned methods, an interesting solution for providing frequency support is investigated in [13], in which inverters can emulate the behavior of synchronous machines, thus being referred to as synchronverters. This technique was successfully applied in a DFIG-based WECS in [14], considering that the grid-side converter (GSC) can be controlled for this purpose. Energy storage devices like batteries connected to the dc link of the back-to-back converter are used to supply the additional power required by the control system. So far, synchronverters have been mostly used in distributed generation and low-power photovoltaic systems [15]. Even though some works focused on the connection of DFIGs to microgrids can be found in the recent literature [16], it is reasonable to state that this is still an incipient subject, especially in terms of studies dedicated to large-size WECSs.

A time-variable droop control that allows VSWTs to support the grid during underfrequency and mitigate secondary frequency dips is presented in [17]. A switching angle controller (SAC) can also be used to regulate the active power output by adjusting the angle between the internal voltage and the terminal voltage of the DFIG as in [18]. The authors in [19] analyzed the influence of the frequency response control on the interaction between the WECS and the grid, proposing a hybrid active damping technique for the WF to mitigate the potential lightly-damped modes. However, this latter solution may not be quite effective when the operation point is not fixed. Distributed model predictive control (DPMC) allows the coordinated operation of the WF and the power grid aiming at frequency control but at the cost of additional complexity involving optimization techniques [20]. Since the virtual inertia control relies on de-loading the WECS because the active power output must increase when the grid frequency is below the rated condition, it is possible to combine it with modern techniques like predictive control and artificial intelligence to obtain the reference quantities for the back-to-back converter [21].

In this context, considering the prominent application of synchronverters to DFIG-based WECSs for frequency support, this work presents a control strategy that relies on replacing the DFIG with a synchronverter, whereas it behaves like a synchronous generator. A thorough performance analysis is also presented while comparing it with other two primary frequency de-loading control techniques, that is, pitch control and SAC. For this purpose, the IEEE 14-bus modified test system available in [22] for steady-state studies is employed, comprising the addition of a 165 MW DFIG-based WF to bus #1 and considering dynamic data for time-domain simulations. The dynamic parameters for a complete synchronous machine model including the machine itself, an exciter, and a regulator are defined based on the Santo Antônio hydroelectric power plant model available in [23], which presents five 82.5 MW generators. The dynamic parameters are also determined for the synchronous compensators according to [24]. The modified test system is thoroughly analyzed in PSCAD/EMTDC environment in terms of the performance of the frequency control techniques.

The remainder of this work is organized as follows. Section 2 presents the modified test system in detail. Section 3 describes the primary frequency control approaches adopted in the comparative analysis, as well as the novel introduced solution based on synchronverters. Sections 4 and 5 discuss the simulation results of the test system associated with the control approaches and main conclusions, respectively.

2. Dynamic model and parameters of the IEEE 14-bus modified test system

Fig. 1 shows the IEEE 14-bus modified test system, where a WF is connected to bus #1. As previously mentioned, data of a real hydropower plant were used for adjusting the generators, including the automatic voltage regulator (AVR) and exciter [23], whereas the synchronous compensators were configured according to [24]. Table 1 shows the parameters associated with the synchronous machines and condensers. Tables 2 and 3 summarize the parameters associated with the DFIGs and transmission lines, respectively.

To adapt the rated voltage of 13.8 kV of the synchronous generators and compensators to the 138 kV system, ideal transformers and buses rated at the same voltage levels of the machines were added to buses #15 – #19. The remaining parameters associated with transmission lines, transformers, voltage levels, and steady-state data are the same as those presented in [24] and [25], resulting in a total system loading of 259 MW and 73.5 Mvar.

The WF connected to bus #1 consists of a 5-MW DFIG with a stator voltage of 690 V, employing a current-controlled rotor-side converter (RSC) based on field-oriented vector control. In turn, the GSC relies on voltage-oriented control. The active switches of both converters are driven using pulse width modulation (PWM) hysteresis control, resulting in a fixed switching frequency of 6 kHz. The DFIG is connected to a 690 V/13.8 kV transformer associated with a 13.8 kV bus, which is used to model a variable-speed WF. A maximum of 33 machines is adopted in the study, resulting in a WF whose total power is 165 MW aiming to replace two synchronous generators connected to bus #1 and keep the total system power constant during the simulation.

The mechanical system, which comprises the turbine and the pitch angle controller, extracts the maximum available power from the wind and produces the mechanical torque. The basic operation principle relies on measuring the wind speed and defining the MPPT curve, which provides an active power reference for the RSC as defined in [26]. To verify the consistency of the modified test system when reflecting real conditions, the short-circuit levels at buses #2 and #5 were calculated, that is, exactly where the frequency is measured and the load blocks are added to verify the power system behavior, respectively.

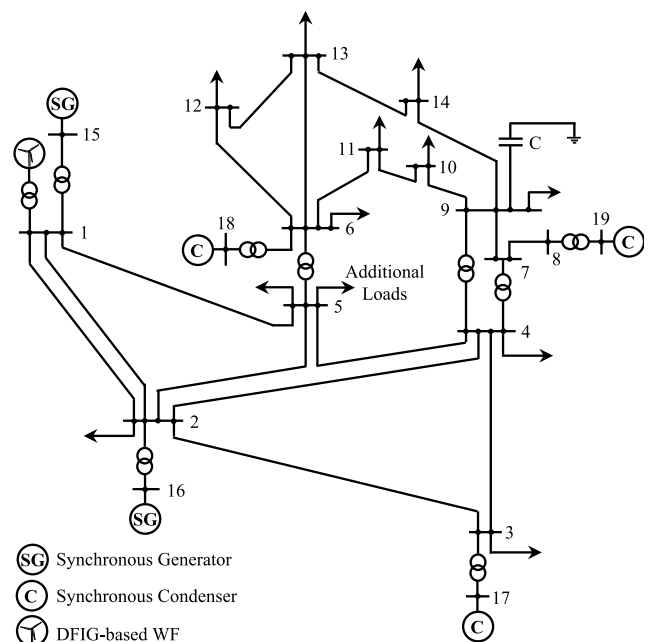According to [27], one can calculate the short-circuit currents

Fig. 1. IEEE 14-bus modified test system.

Table 1
Parameters of synchronous generators and condensers.

Operation	Sync. Gen.	Sync. Gen.	Condenser	Condenser
Default Unit no. (New Unit no.)	1 (15)	2 (16)	3 (17)	6 (18), 8 (19)
Rated Power (MVA)	247.5	165	40	25
Rated Voltage (kV)	13.8	13.8	13.8	13.8
H(s)	3.600	3.600	1.520	1.200
r_a(s)	0.002	0.003	0.000	0.003
x_d (pu)	0.333	0.500	2.373	1.769
x_q (pu)	0.220	0.330	1.172	0.580
x_d' (pu)	0.123	0.185	0.343	0.304
x_q' (pu)	0.153	0.230	1.172	0.228
x_d'' (pu))	0.097	0.145	0.231	0.204
x_q'' (pu)	0.097	0.145	0.231	0.204
x_p (pu)	0.053	0.080	0.132	0.105
T_{do}' (s)	5.700	5.700	11.600	8.000
T_{qo}' (s)	0.135	0.135	0.850	0.850
T_{do}'' (s)	0.050	0.050	0.058	0.053
T_{qo}'' (s)	0.120	0.120	0.201	0.015

Table 2
DFIG parameters.

Parameter	Value
Rated active power	$P_n = 5$ MW
Rated line-to-line stator voltage	$V_{sLL} = 0.69$ kV
Turns ratio between the stator and rotor	0.3
Rated frequency	$f = 60$ Hz
Stator resistance	$R_s = 0.0054$ pu
Stator leakage inductance	$L_{ls} = 0.1$ pu
Rotor resistance	$R_r = 0.00607$ pu
Rotor leakage inductance	$L_{lr} = 0.11$ pu
Magnetizing inductance	$L_m = 4.5$ pu
Angular moment of inertia	$J = 6$ s
Grid-side coupling inductance	$L_g = 0.126$ mH
Rated dc-link voltage	$V_{dc} = 1.45$ kV
Dc-link capacitor	$C_{dc} = 15$ mF
Wind speed at the maximum power coefficient ($C_{p(max)}$)	$V_{w(base)} = 11$ m/s
Rated mechanical output power	$P_{mec} = 5$ MW
Turbine initial speed	$\omega_0 = 1.2$ pu

Table 3
Parameters of transmission lines.

Line From bus #	To bus #	R [pu/m]	X [pu/m]	B [pu/m]
1	2	0.0194	0.0592	0.0528
1	5	0.054	0.223	0.0492
2	3	0.047	0.198	0.0438
2	4	0.0581	0.176	0.034
2	5	0.057	0.174	0.0346
3	4	0.067	0.171	0.0128
4	5	0.0134	0.0421	0.0001
6	11	0.095	0.199	0.0001
6	12	0.123	0.256	0.0001
6	13	0.0662	0.13	0.0001
7	8	0.0001	0.176	0.0001
7	9	0.0001	0.11	0.0001
9	10	0.0318	0.0845	0.0001
9	14	0.127	0.27	0.0001
10	11	0.0821	0.192	0.0001
12	13	0.221	0.2	0.0001
13	14	0.171	0.348	0.0001

through the buses using symmetrical components and sequence impedances. The following assumptions are made for calculating the equivalent Thévenin impedances: the generators are represented by their respective d-axis subtransient reactances x_d''; the transmission lines are represented in terms of the pi model; the load power is constant and not taken into account for simplicity; the transformers are represented

by their respective total leakage reactances.

One can determine the short-circuit level (SCL) of a given bus by obtaining the equivalent Thévenin representation of the system as in (1), where V_{Th} is the Thévenin voltage and Z_{Th} is the impedance seen from the bus where the short circuit occurs, respectively.

$$SCL = \frac{V_{Th}^2}{Z_{Th}}. \tag{1}$$

Considering a balanced three-phase system, the positive-sequence impedances of the circuit components are equal to their respective real parts. From the bus impedance matrix $\dot{Z}$, one can determine the equivalent impedances of the whole system from the inverse nodal admittance matrix $\dot{Y}^{-1}$ as in (2).

$$\dot{Z} = \dot{Y}^{-1} = \begin{bmatrix} \dot{Z}_{11} & \dot{Z}_{12} & \dots & \dot{Z}_{1n} \\ \dot{Z}_{21} & \dot{Z}_{22} & \cdots & \dot{Z}_{2n} \\ \vdots & \vdots & \vdots & \vdots \\ \dot{Z}_{m1} & \dot{Z}_{m2} & \dots & \dot{Z}_{mn} \end{bmatrix}, \tag{2}$$

where Z_{mn} is the impedance associated with two buses m and n, respectively.

Considering the parameters listed in Table 1 – Table 3 and using the aforementioned methodology, one can obtain the Thévenin impedances associated with buses #2 and #5 as $Z_{22} = 0.0035 + j0.0455$ pu and $Z_{55} = 0.0148 + j0.0851$ pu, respectively. Thus, the respective three-phase short-circuit currents are $I_{sc2} = 9.158$ kA and $I_{sc5} = 4.843$ kA. Considering $V_{Th} = 1$ pu in (1), the SCLs of buses #2 and #5 are 2188.2 pu and 1157.4 pu, respectively. One can also determine the short-circuit ratio (SCR) from (3) for an available power $P_d = 411.25$ MW, resulting in $SCR_2 = 5.32$ and $SCR_5 = 2.81$. Fig. 2 shows the behavior of the root mean square (RMS) three-phase short-circuits, which were obtained from the model implemented in PSCAD environment. It is observed that I_{sc2} and I_{sc5} correspond exactly to the calculated values.

$$SCR = \frac{SCL}{P_d} \tag{3}$$

An increase of the load power was simulated in bus #5 without considering the WF to assess the impact on the grid frequency. The loading increases at instant $t = 40$ s, exactly when the start-up transient of the power system and synchronous generators finishes. Table 4 presents the load added to bus #5 for distinct scenarios in absolute values and as a percentage of the total system loading of 259 MW and 73.5 Mvar. Fig. 3 also presents the behavior of the system frequency measured on bus #2 for scenario #4. The frequency reduces up to 57.12 Hz, increases to 59.44 Hz after 50 s, and equals 58.5 Hz at $t = 53.86$ s, that is, 13.86 s after the load step. Considering that the maximum time interval between 56 Hz and 58.5 Hz is 20 s, this is the worst-case scenario for which the underfrequency protection is not enabled. Therefore, this condition will be adopted in the forthcoming analysis.

The rate of change of frequency (RoCoF) is defined as the derivative of the power system frequency over time (df/dt) measured when load-
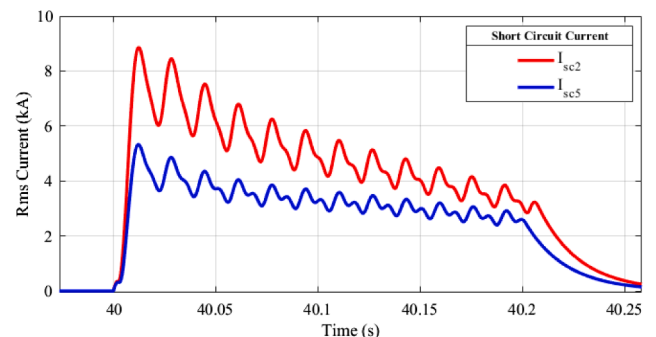

Fig. 2. RMS three-phase short-circuit currents through buses #2 and #5.

Table 4
Load step in bus #5.

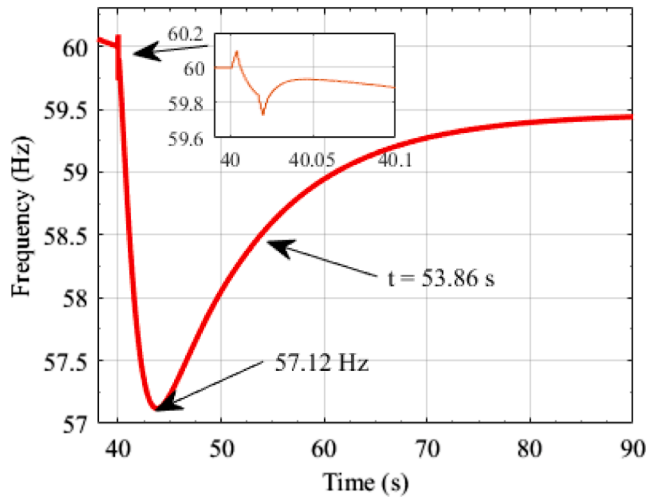| Scenario	Load step (MW / Mvar)	Load step (%MW /%Mvar)
1	9 / 3	3.47 / 4.08
2	15 / 3	5.79 / 4.08
3	30 / 6	11.58 / 8.16
4	60 / 12	23.16 / 16.32
5	90 / 15	34.75 / 20.41

Fig. 3. Frequency deviation after the load step.

generation imbalances occur as caused by the disconnection of either large loads or generators, or by system splits. This is an important parameter that reflects the grid robustness and can be calculated from (4) [28].

$$\text{RoCoF}|_{t=0^+} = \frac{\Delta P_{imb}}{P_{load}} \frac{f_o}{2H}, \tag{4}$$

where 0^+ denotes the instant after the load-generation disconnection, ΔP_{imb} represents the load-generation variation, P_{load} is the total load power, f_0 is the system frequency before the disconnection, and H is the equivalent inertia of the system in seconds.

The careful analysis of (4) reveals that the low values of SCL_2 and SCL_5 as associated with SCR_2 and SCR_5, respectively imply a low inertia H, thus causing the term $f_0/2H$ to be high. Besides, a power variation of 60 MW/12 Mvar for scenario #4 considering a total loading of 412.5 MW causes $\Delta P_{imb}/P_{load}$ to be high as well in (4), resulting in a high value of RoCoF. This is the main reason why the frequency drops significantly in Fig. 3. Thus, it is reasonable to assume that the system frequency may vary from 60 Hz to 57.12 Hz in practice, this being a benchmark for the present study and future work on frequency variation.

3. Frequency control techniques for DFIGs

The classical modeling of DFIG-based systems composed of back-to-back converters is well known in the literature. From the simplified analytical model of the machine described in [29], one can obtain (5) – (8) for the representation in the *dq* reference frame.

$$v_{sd} = R_s i_{sd} + \frac{d\psi_{sd}}{dt} - \omega_s \psi_{sq}, \tag{5}$$

$$v_{sq} = R_s i_{sq} + \frac{d\psi_{sq}}{dt} + \omega_s \psi_{sd}, \tag{6}$$

$$v_{rd} = R_r i_{rd} + \frac{d\psi_{rd}}{dt} - \omega_{sl} \psi_{rq}, \tag{7}$$

$$v_{rq} = R_r i_{rq} + \frac{d\psi_{rd}}{dt} - \omega_{sl} \psi_{rd}, \tag{8}$$

where v, i, R, ψ, and ω represent the voltage, current, resistance, magnetic flux, and angular speed, respectively; d and q stand for quantities associated with the direct and quadrature axes; respectively; r and s correspond to quantities associated with the rotor and stator, respectively; and ω_{sl} is the slip angular frequency.

Manipulating (5) – (8) and considering the stator and rotor magnetic fluxes expressed in terms of the *dq* currents and inductances L, one can obtain the stator currents I_{sd} and I_{sq} as a function of the rotor currents I_{rd} and I_{rq} from (9) and (10), respectively. Thus, it is possible to control the stator current components from I_{rd} and I_{rq}, and consequently the active and reactive power of the machine.

$$I_{sd} = \frac{\omega_s L_s V_{sq}}{(\omega_s^2 L_s + 2sR_s + s^2 L_s)L_s} - \frac{L_m I_{rd}}{L_s}, \tag{9}$$

$$I_{sq} = \frac{(R_s + sL_s)V_{sq}}{(\omega_s^2 L_s + 2sR_s + s^2 L_s)L_s} - \frac{L_m I_{rq}}{L_s}, \tag{10}$$

where L_m is the magnetizing inductance.

The classical control methods of DFIGs employ the RSC to define the active and reactive power using field-oriented vector control. The stator active power P_s and stator reactive power Q_s can be calculated from (11) and (12), respectively.

$$P_s = v_{sd} i_{sd} + v_{sq} i_{sq}, \tag{11}$$

$$Q_s = v_{sq} i_{sd} - v_{sd} i_{sq}. \tag{12}$$

Substituting (9) and (10) after converting the quantities from the Laplace domain to the *dq* reference frame in (11) and (12), it is possible to obtain the stator reference currents $i_{rd}*$ and $i_{rq}*$ for the RSC from (13) and (14), respectively, as demonstrated in [29].

$$i_{rd}* = \frac{v_{sq}^2 - Q_s^* \omega_s L_s}{v_{sq} \omega_s L_m}, \tag{13}$$

$$i_{rq}* = \frac{-P_s^* L_s}{v_{sq} L_m}, \tag{14}$$

where "*" denotes reference values.

The GSC is responsible for regulating the dc-link voltage and the reactive power flow through the back-to-back converter. Using voltage-oriented control, it is possible to define the voltages at the point of common coupling (PCC) denoted by v_{PCC} as a function of the voltages in the *dq* reference frame from (15) and (16), respectively.

$$v_{PCCd} = R i_d + L \frac{di_d}{dt} - \omega_s L i_q + v_{invd}, \tag{15}$$

$$v_{PCCq} = R i_q + L \frac{di_q}{dt} - \omega_s L i_d + v_{invq}, \tag{16}$$

where v_{invd} and v_{invd} are the *d*-axis and *q*-axis components of the GSC voltages.

Manipulating (15) and (16), as well as assuming $v_{PCC}=v_{PCCd}$ and $v_{PCCq} = 0$, one can obtain the reference voltages for the GSC in (17) and (18).

$$v_{invd}* = v_{PCCd} - R i_d + L \frac{di_d}{dt} + \omega_s L i_q, \tag{17}$$

$$v_{invq}* = -\left(R i_q + L \frac{di_q}{dt} + \omega_s L i_d \right). \tag{18}$$

To solve frequency stability issues of interconnected power systems caused by the high penetration of VSWTs such as DFIG-based ones, two types of frequency control strategies have often been adopted in the

literature. The first group of control methods allows WFs to participate in primary frequency control by operating with a low power output (de-loading), reserving part of the active power for other tasks than MPPT. For this purpose, overspeed techniques [30] and pitch angle control [31] are used. The second group comprises the so-called virtual inertia control, in which wind turbines emulate the behavior of synchronous generators during frequency variation events. Such approaches can be divided into three main categories [32]: Δf response, which depends on the deviation in the system frequency from the rated value, with adjustable parameters and strategies that define the type of response; ii) fixed trajectory response, this being a decoupled strategy in which a fixed response is enabled for any frequency deviation beyond a given threshold; and iii) df/dt response, which is enabled by the instantaneous RoCoF, thus emulating an inertia-type synchronous response.

To evaluate the performance of de-loading methods, two distinct approaches are addressed as follows: the first one combines inertia and pitch angle control [33], whereas the second one comprises the association of SAC and automatic generator controller (AGC) [18]. In turn, the method proposed in this work relies on emulating the behavior of a synchronous generator by applying the synchronverter concept for controlling the GSC, whereas it is not a de-loading-based approach. In other words, the power required by the system is supplied by a battery bank connected in parallel with the dc-link capacitor. This is a very interesting solution, especially considering that the generator will always operate at the maximum power point. Besides, there is no need for mechanical components, thus making the dynamic response of the control system very fast owing to the battery bank.

Fig. 4 presents the modified control system of a DFIG-based WECS that incorporates the primary frequency control as an ancillary service.

It is worth mentioning that the synchronverter-based control is supposed to replace conventional vector control solutions typically used in WECSs.

3.1. Pitch angle control

This technique relies on de-loading the WECS to increase the pitch angle β so that part of the rated active power can be used for frequency support. Droop control can be used to adjust the reserve active power margin ΔP as a function of the frequency variation Δf according to (19) [34]. The power versus frequency characteristic of a droop control system is shown in Fig. 5.
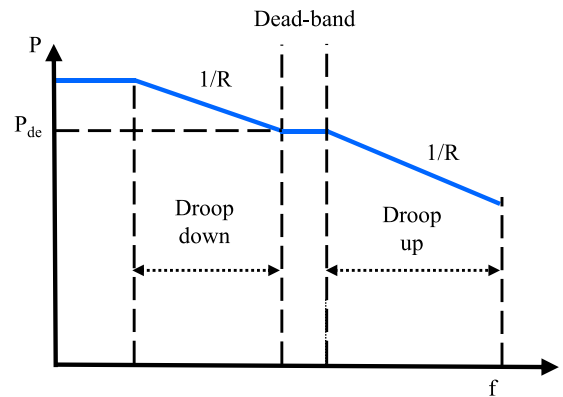

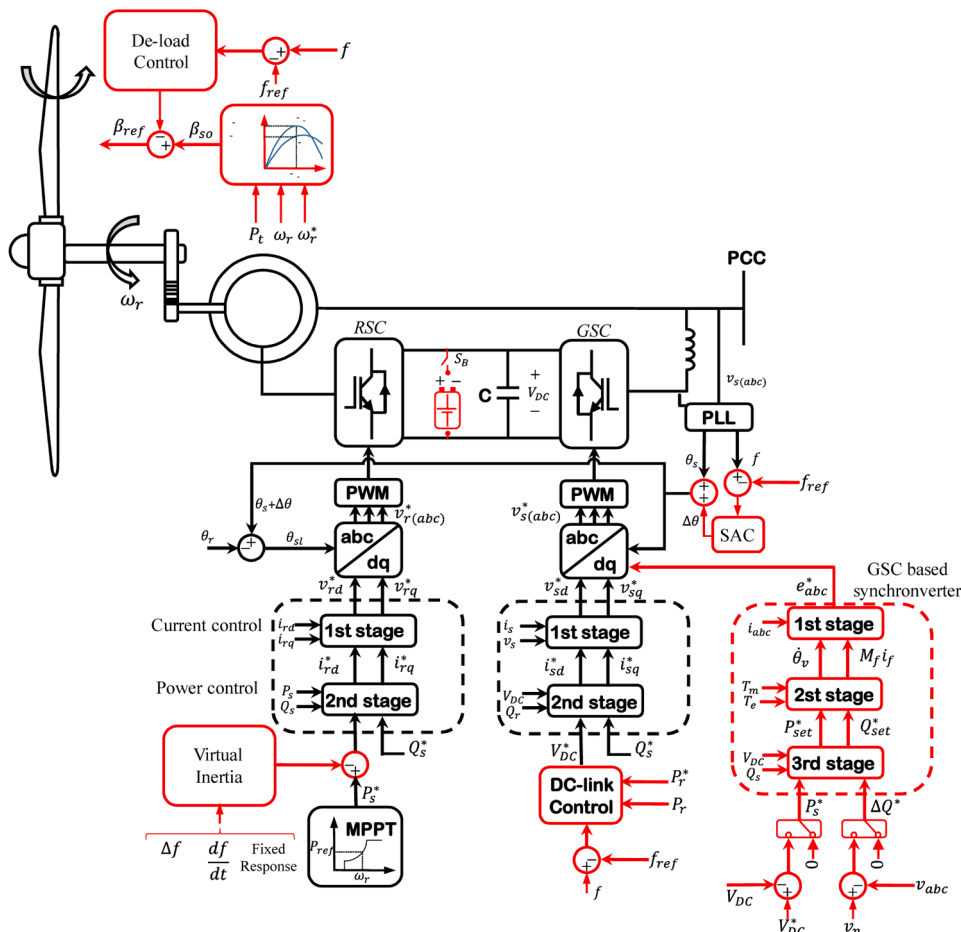Fig. 5. Droop characteristic of frequency control.

Fig. 4. Typical control system of a DFIG-based WECS with primary frequency control.

$$\Delta P = -K_G \Delta f, \tag{19}$$

where the power regulation coefficient is equal to the inverse of parameter R as defined by (20).

$$R = \frac{1}{K_G} = \frac{\Delta f}{\Delta P}. \tag{20}$$

Fig. 6 shows the power P_e versus rotor angular velocity ω_r characteristic of the DFIG simulated in this work, as well as the maximum power point for a pitch angle $\beta_0=0°$. When the angle changes to $\beta_1 = 2°$, the power curve also does, reducing the maximum power of the machine for the same wind speed. The difference between the maximum power P_{MPPT} and the new de-loaded power P_{de} represents the wind turbine power margin to be used during frequency variation events, thus emulating the droop control of synchronous machines. It is observed that the maximum power is 1.0 pu at $\omega_r = 1.1$ pu for $\beta_0 = 0°$. When the pitch angle is $\beta_1 = 2°$, the de-loaded power is 0.832 pu, representing a difference of 0.168 pu or 845 kW in the case of a 5 MW DFIG.

Fig. 7 presents the pitch angle controller described in [33], where the pitch angle is controlled at a rate of 2° per second in the event of a system frequency variation Δf. The relationship between the pitch angle variation $\Delta\beta$ and Δf can be expressed by (21).

$$\Delta\beta = K_\beta \Delta f = K_\beta \left(f_{meas} - f_{ref} \right), \tag{21}$$

where K_β is a proportional coefficient; f_{meas} and f_{ref} are the measured and reference values of the system frequency, respectively.

The relationship between P_{de} and P_{MPPT} can be expressed by (22), where $K\%$ is a percent coefficient.

$$P_{de} = \left(1 - \frac{K\%}{100} \right) P_{MPPT}. \tag{22}$$

The controller shown in Fig. 7 was incorporated into the WF considering the IEEE 14-bus modified test system for verifying the performance during frequency events. It is worth mentioning that this technique may prove to be slower than the virtual inertia control owing to the need for changing the pitch angle, this task being assigned to auxiliary motors coupled to mechanical reducers for turning the blades. In real projects, the usual angle rotation speed is between 1 and 5° per second, being faster for small angles and slower as β increases. In this study, the initial pitch angle is adjusted to 2° to reduce the initial output power. The speed of rotation of the blades is 2° per second.

3.2. SAC

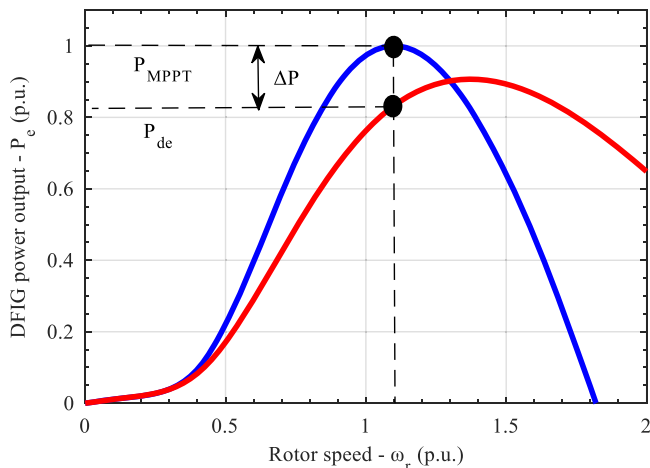This strategy was formerly proposed in [33] and relies on de-loading

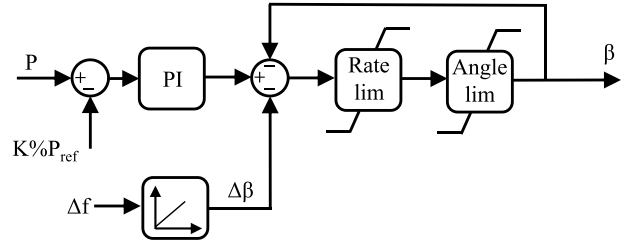**Fig. 6.** DFIG power curves for different pitch angles.

Fig. 7. Block diagram of the pitch angle control.

the wind turbine similarly to the pitch angle control, but aiming to obtain a given power margin for controlling the switching angle instead. This controller is associated with an adder, whose inputs are the stator phase angle measured by a phase-locked loop (PLL) and a virtual rotor angle generated by the SAC. The resulting sum is applied to the controllers of the GSC and RSC, thus increasing the power output of the wind turbine. In other words, this technique causes the DFIG to behave like a synchronous generator.

SAC is a discrete controller with only two control inputs. The active power output is adjusted by controlling the angle between the internal voltage and the terminal voltage of the DFIG, which is called virtual rotor angle. In this way, the response to frequency deviations with active power support is faster than that of continuous controllers. Continuous controllers can respond to changes over a wide frequency range, whereas SAC can only be enabled when the frequency deviation exceeds a specific threshold. Therefore, SAC is more robust to small magnitude oscillations and measurement noise associated with the system frequency.

The equivalent Thévenin circuit that represents the DFIG is shown in Fig. 8(a), where R_{eq} and L_{eq} are the equivalent resistance and inductance, respectively, and $\vec{V}_s$ is the stator voltage. Thus, one can calculate the internal voltage $\vec{E}_{ms}$ from (23).

$$\vec{E}_{ms} = \frac{s\omega_s^2 L_m L_r + j\omega_s L_m R_r}{R_r^2 + (s\omega_s L_r)^2}. \tag{23}$$

Assuming that $\vec{V}_s = V_s\angle\theta_s$ and $\vec{E}_{ms} = E_{ms}\angle(\theta + \theta_s)$, where V_s and E_{ms} are the absolute values of the stator voltage and terminal voltage, respectively, θ is the DFIG virtual angle, and θ_s is the stator voltage angle, one can obtain the active power transferred from E_{ms} to V_s as in (24).

$$P_e = \frac{V_s}{\sqrt{R_{eq}^2 + X_{eq}^2}} \left[R_{eq}(E_{ms}\cos\theta - V_s) + X_{eq}E_{ms}\sin\theta \right] \tag{24}$$

Since $X_{eq} \gg R_{eq}$ during the normal operation of the DFIG, one can simplify (24) as (25).

$$P_e = \frac{E_{ms}V_s}{X_{eq}}\sin\theta. \tag{25}$$

Fig. 9 shows the behavior of the virtual rotor angle θ as a function of P_e. When the system frequency drops, one can increment the DFIG active power by increasing θ. Fig. 10 presents the controller block diagram, which is responsible for generating an angle $\Delta\theta$.
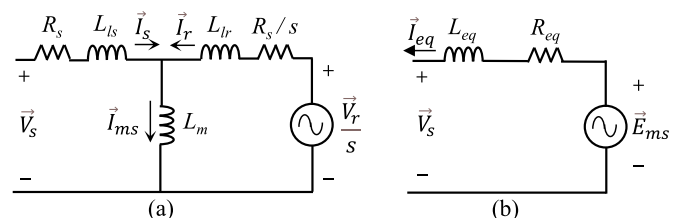

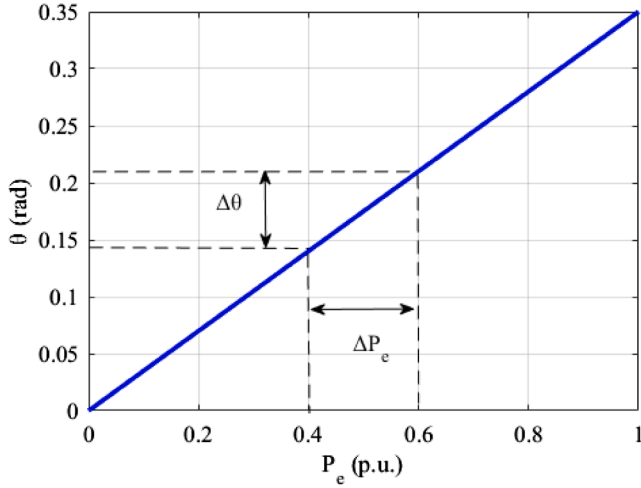**Fig. 8.** Equivalent circuit of the DFIG in a steady-state condition.

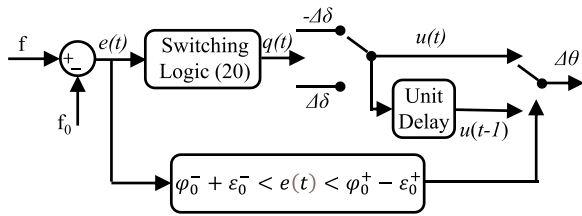**Fig. 9.** Virtual rotor angle θ as a function of the active power P_e in a DFIG-based WECS.

Fig. 10. Block diagram of the SAC.

As previously mentioned, the SAC is designed to operate with two control inputs, namely the increment and decrement of an angle represented by $+\Delta\delta$ and $-\Delta\delta$, respectively. To maintain the stable operation of the DFIG, the virtual rotor angle θ must always be positive. The SAC input is the frequency deviation $f-f_0$, where f is the load frequency and f_0 is the rated system frequency. The switching logic is represented by (26).

$$u(t) = \begin{cases} u(t-1), \text{if} e(t) \in (\varphi_0{}^- + \varepsilon_0{}^-, \varphi_0{}^+ - \varepsilon_0{}^+) \\ u(t), \text{if} e(t) \leq \varphi_0{}^- + \varepsilon_0{}^- \vee e(t) \geq \varphi_0{}^+ - \varepsilon_0{}^+ \end{cases}. \tag{28}$$

In other words, if the frequency error is within the trigger limits, the SAC output will correspond to $u(t)$ as associated with a given time delay. If the thresholds are reached, the output becomes $u(t)$. This prevents unwanted excursions of $\Delta\delta$ in case of instantaneous frequency variations beyond limits. The controller output is added to the phase angle θ_{PLL} measured by the PLL of the DFIG. The resulting phase angle is then used to generate the three-phase voltage references for the PWM modules of the RSC and GSC.

To increase the power output when the frequency varies, the DFIG must operate in a steady state with a reduced power reference, similarly to the behavior of the pitch control method. The power margin adopted in this case is 16.8%, which corresponds to an angle $\beta_1 = 2°$ as defined previously, resulting in a power reference of 0.832 pu.

3.3. Synchronverter-based control of the GSC

The term "synchronverter" was first defined in [13], which stated that an inverter is capable of emulating a synchronous generator. Thus, the control theory related to synchronous generators can be promptly applied in grid-tied inverters. One can then control the active and reactive power supplied by synchronverters to emulate the well-known frequency and voltage droop mechanisms. In this work, a synchronverter is used to replace the traditional vector control associated with the GSC. Similarly, the authors in [35] employed synchronverters combined with theRSC. However, such a solution does not rely on additional energy sources and a PLL is not necessary. The results evidence that the power reservation is somewhat limited because the only energy source is the dc-link capacitor, whose voltage should be properly controlled. In turn, the present study incorporates a battery bank in parallel with the dc link to provide frequency support, considering that an additional amount of energy is injected into the PCC through the GSC. Therefore, this process will not affect the stability of the RSC, whose control system requires a PLL.

The first step consists in modeling the synchronous machine, this being a well-known process in the literature that comprises the electrical and mechanical parts. The model described in [13] and updated in [35]

$$q(t) = \varsigma(e(t), \varphi_0{}^+ - \varepsilon_0{}^+, \varphi_0{}^- + \varepsilon_0{}^-, q(t-)) = [e(t) \geq \varphi_0{}^+ - \varepsilon_0{}^+ \vee ((t) \geq \varphi_0{}^+ + \varepsilon_0{}^+ \wedge q(t-))]$$
$$q(0-) \in \{\text{true}, \text{false}\}, \tag{26}$$

where $q(t)$ is the output of switching logic ς, which can be true of false; $e(t) = f - f_0$ is the error corresponding to the frequency deviation; $\varphi_0{}^+$ and $\varepsilon_0{}^+$ are constant values measured in hertz, used to define the funnel error $\mathscr{F}_0 := \{(t, e(t)) \in *R*_{\geq 0} \times *R*|\varphi_0{}^- \leq e(t) \leq \varphi_0{}^+\}$; $\vee$ and $\wedge$ are the OR and AND operators, respectively; $q(t-) = \lim_{t\to 0+} q(t-\varepsilon)$; $\varphi_0{}^- + \varepsilon_0{}^-$ and $\varphi_0{}^+ - \varepsilon_0{}^+$ are the lower and upper thresholds of a switching event, respectively. Therefore, the switching of $q(t)$ does only occur when $e(t) = \varphi_0{}^- + \varepsilon_0{}^-$ or $e(t) = \varphi_0{}^- + \varepsilon_0{}^-$, as there is no sliding mode.

The control law $u(t)$ associated with $q(t)$ is defined by (27).

$$u(t) = \begin{cases} -\Delta\delta \text{if} q(t) = \text{true} \\ +\Delta\delta \text{if} q(t) = \text{false} \end{cases}. \tag{27}$$

The analysis of (26) and (27) shows that SAC cannot generate a neutral value like $u(t) = 0$. However, the controller output, that is, the virtual angle θ must be constant in a steady state. Therefore, the conditional delay block represented by (28) is incorporated into the respective block diagram.

was used for this purpose. Considering the ideal representation in Fig. 11 (a), one can state that the mutual inductances between the field winding and the stator windings vary according to the rotor electrical angle θ as in (29).

$$\begin{cases} M_{af} = M_f\cos(\theta) \\ M_{bf} = M_f\cos\left(\theta - \frac{2\pi}{3}\right), \\ M_{cf} = M_f\cos\left(\theta - \frac{4\pi}{3}\right) \end{cases} \tag{29}$$

where M_f is the amplitude of the mutual inductance.

Considering that M is the mutual inductance between the windings, one can obtain the equations for representing the flux linkages ϕ of the armature phases a, b, and c and the field winding f according to (30).
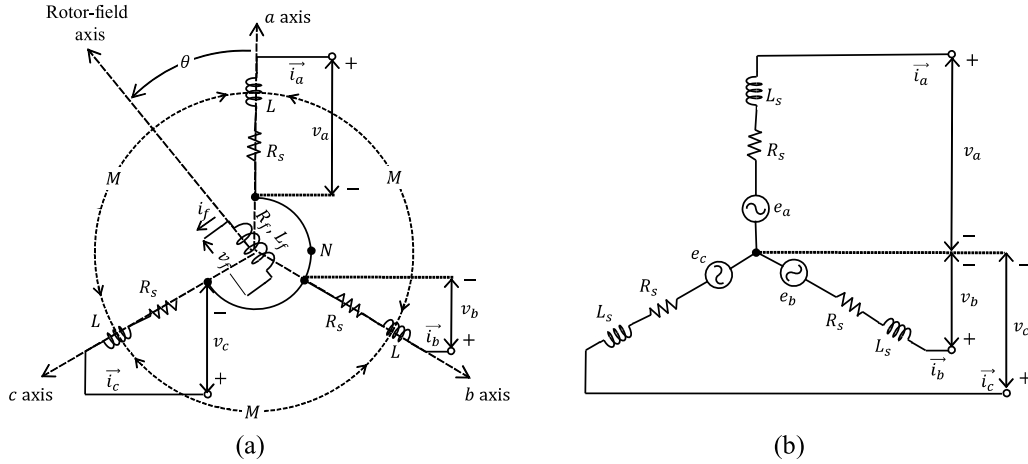
Fig. 11. (a) Ideal representation of a three-phase synchronous generator considering one pole pair ($p = 1$) and (b) its respective equivalent circuit.

$$\begin{cases} \phi_a = Li_a - Mi_b - Mi_c + M_{af}i_f \\ \phi_b = -Mi_a + Li_b - Mi_c + M_{bf}i_f \\ \phi_c = -Mi_a - Mi_b + Li_c + M_{cf}i_f \\ \phi_f = M_{af}i_a + M_{bf}i_b + M_{cf}i_c + L_f i_f \end{cases}, \tag{30}$$

where i_a, i_b, i_c are the stator currents and i_f is the rotor excitation current.

One can assume that the neutral remains unconnected, that is, $i_a + i_b + i_c = 0$, as well as adopt a vector notation according to (31) to (34).

$$\Phi = \begin{bmatrix} \phi_a \\ \phi_b \\ \phi_c \end{bmatrix}, \tag{31}$$

$$i = \begin{bmatrix} i_a \\ i_b \\ i_c \end{bmatrix}, \tag{32}$$

$$cos(\theta) = \begin{bmatrix} \cos(\theta) \\ \cos\left(\theta - \dfrac{2\pi}{3}\right) \\ \cos\left(\theta - \dfrac{4\pi}{3}\right) \end{bmatrix}, \tag{33}$$

$$sin(\theta) = \begin{bmatrix} \sin(\theta) \\ \sin\left(\theta - \dfrac{2\pi}{3}\right) \\ \sin\left(\theta - \dfrac{4\pi}{3}\right) \end{bmatrix}. \tag{34}$$

Thus, one can represent the stator flux linkage as in (35).

$$\Phi = L_s i + M_f i_f cos(\theta), \tag{35}$$

where:

$$L_s = L + M. \tag{36}$$

In turn, the flux linkage in the field winding can be written as in (37).

$$\phi_f = L_f i_f + M_f \langle i, cos(\theta) \rangle, \tag{37}$$

where $\langle, \rangle$ denotes the inner product between the variables. Thus, it is observed that the second term of the sum in (37) is constant if the phase currents are sinusoidal and balanced.

Now, considering the equivalent circuit in Fig. 11(b), the phase voltages $v = \begin{bmatrix} v_a & v_b & v_c \end{bmatrix}^\mathrm{T}$ are obtained from (35), resulting in (38).

$$v = -R_s i - \frac{d\Phi}{dt} = -R_s i - L_s \frac{di}{dt} + e, \tag{38}$$

where $e = \begin{bmatrix} e_a & e_b & e_c \end{bmatrix}^\mathrm{T}$ is the electromotive force (emf) due to the rotor as calculated from (39).

$$e = M_f i_f \dot{\theta} sin(\theta) - M_f \frac{di_f}{dt} cos(\theta), \tag{39}$$

where $\dot{\theta}$ is the first-order derivative of the rotor electrical angle with respect to time.

Assuming that the excitation current is constant, one can obtain (40).

$$\overrightarrow{e}_{abc} = M_f i_f \dot{\theta} sin(\theta) \tag{40}$$

The mechanical model of the synchronous generator is related to the swing equation as in (41).

$$J\ddot{\theta} = T_m - T_e - D_p \dot{\theta}, \tag{41}$$

where J is the moment of inertia of all the moving parts associated with the rotor, $\ddot{\theta}$ is the first-order derivative of the angular speed with respect to time, T_m is the mechanical torque, T_e is the electromagnetic torque, and D_p is the damping factor. It is worth mentioning that one can calculate T_e from (42) as demonstrated in [35].

$$T_e = M_f i_f \langle i, sin(\theta) \rangle. \tag{42}$$

Assuming that i_f is constant, manipulating (39) and (42) gives (43).

$$T_e \dot{\theta} = \langle i, e \rangle. \tag{43}$$

The operating principle demonstrated so far is now applied to the synchronverter represented in Fig. 12. It consists of a conventional three-phase dc-ac converter employing insulated gate bipolar transistors (IGBTs). An output low-pass filter is connected to the system phases to mitigate the harmonic content due to the high-frequency operation of the semiconductors. The filter impedance is composed of the resistance R_s and inductance L_s, corresponding to the impedance of the armature windings of the emulated synchronous generator. The voltages generated by the converter are e_{abc}, whereas v_{abc} are the voltages across the filter capacitors defined in (38).

The control system is implemented based on the mathematical model of the synchronous generator. Fig. 13 shows the proposed architecture associated with the GSC, which comprises the frequency and voltage droop control and dc-link voltage regulation. The interaction between the power and control stages occurs through signals e_{abc} and i_{abc}, as well as the voltages synthesized by the synchronverter corresponding to v_{abc} and the grid voltages v_{ga}, v_{gb}, v_{gc}. Thus, the state variables of the synchronverter are the actual currents i_{abc}, and parameters θ_v and $\dot{\theta}_v$, corresponding to the virtual angles and virtual angular speed equivalent to angle θ in the synchronous generator, respectively. The term "virtual"
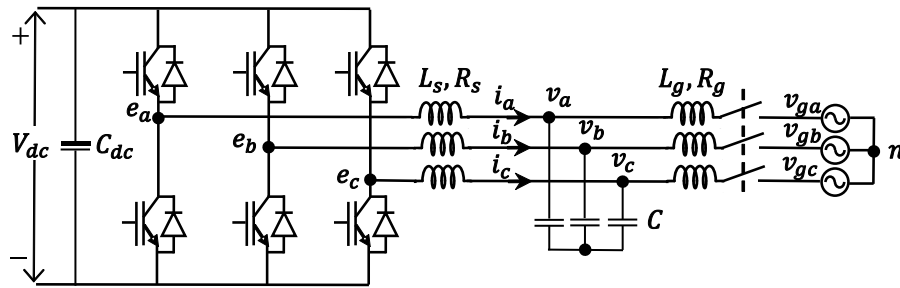
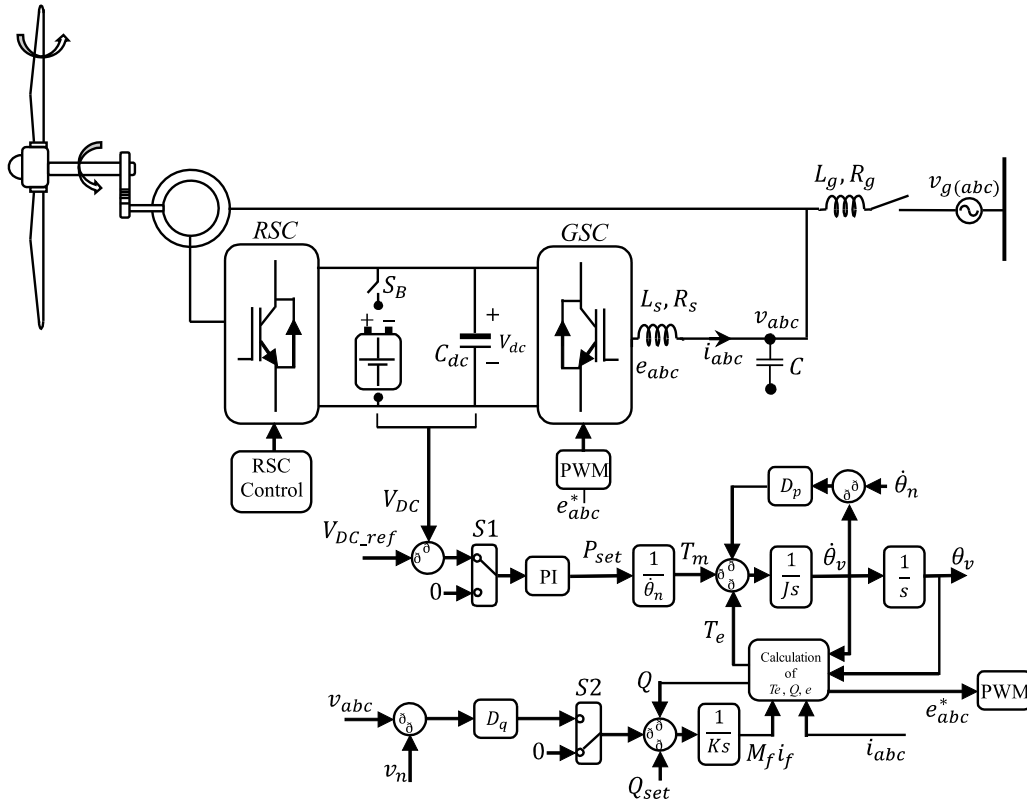**Fig. 12.** Power stage of a synchronverter.

Fig. 13. Schematic of the DFIG control system with the synchronverter associated with the GSC.

refers to the fact that the angle is defined by the control system instead of the machine. The control inputs are T_m and $M_f i_f$, whereas an additional loop is responsible for generating the $M_f i_f$ signals and controlling the reactive power Q_{set}. In turn, one can obtain T_m by dividing the reference active power P_{set} by the rated angular speed $\dot{\theta}_n$. Thus, one can maintain the system stability while ensuring the desired values of the active and reactive powers.

One of the main characteristics of synchronous generators is the capacity to vary the supplied active power according to the grid frequency, which is referred to as frequency droop. When the required active power increases, the speed regulator increases the mechanical power to compensate for the drop in the machine speed as a consequence of the increase of T_e in (41). This mechanism is incorporated into the synchronverter by comparing the virtual angular speed $\dot{\theta}_v$ with the rated angular speed $\dot{\theta}_n$, the difference between them being the input of the damping block D_p. As a result, the damping factor behaves as a frequency droop coefficient defined as the ratio between the required torque variation ΔT for varying the active power and the angular speed variation $\Delta\dot{\theta}_v$, resulting in (44).

$$D_p = \frac{\Delta T}{\Delta \dot{\theta}_v}. \tag{44}$$

The active torque reference is obtained from the ratio between P_{set} and the rated mechanical angular speed. Since the synchronverter does not contain moving parts, the latter parameter becomes equal to $\dot{\theta}_n$. Thus, the active power control loop behaves as a cascade structure, in which the inner and outer loops are associated with the frequency (speed) and active power (torque) in Fig. 13, respectively. The time constant of the frequency loop τ_f is also directly related to J in (45).

$$J = D_p \tau_f. \tag{45}$$

Since there is no delay involved in the frequency loop, the time constant τ_f can be much less than that of a real synchronous generator, thus ensuring fast reference tracking. Therefore, for a given value of the frequency droop coefficient D_p, J must be small. However, this issue is not a contradiction considering the typically high inertia of an actual synchronous machine, because J now becomes a mathematical control variable independent of the inertia. Thus, one can obtain short-term energy storage in the synchronverter using storage devices like batteries.

A third loop can be associated with the DFIG to regulate the dc-link voltage V_{dc}. Similarly to vector control, it remains constant at a given reference value $V_{dc(ref)}$ using a proportional-integral (PI) controller, which is responsible for generating P_{set}. The main difference is that the conventional vector control generates a reference current instead. For this purpose, the quantities should be properly adjusted, considering that switch $S1$ in Fig. 13 will be turned off when a frequency dip occurs. Under this condition, the synchronverter starts operating in frequency support mode, no longer regulating the dc-link voltage. Besides, switch S_B must be turned on at the same time to connect the battery bank in parallel with the dc link.

The reactive power is controlled similarly to the active power in terms of the voltage droop control. One can define the voltage droop coefficient D_q in (46) as the ratio between the reactive power variation ΔQ and the voltage variation across the synchronverter terminals given by ΔV.

$$D_q = \frac{\Delta Q}{\Delta V}. \qquad (46)$$

The reactive power control loop is represented in the bottom part of Fig. 13. The difference between the maximum rated voltage v_n and the grid voltage v_{abc} is multiplied by D_q and added to the difference between the reference and actual values of the reactive power given by Q_{set} and Q, respectively. The resulting signal is applied to an integrator whose gain is $1/K$, generating the control signal $M_f i_f$. Thus, the reactive power regulation mechanism also consists of a cascade structure, in which the inner and outer loops are responsible for controlling the voltage and reactive power, respectively. One can also calculate constant K from (47).

$$K = \dot{\theta}_n D_q \tau_v, \qquad (47)$$

where τ_v is the time constant of the voltage control loop. It is worth mentioning that one can disable the voltage control loop by turning off switch $S2$ in Fig. 13. Thus, the synchronverter will control only the reactive power while trying to maintain the reference value, which is often set to $Q_{set} = 0$.

One important aspect related to the control approach described so far is the proper tuning of PI controllers while taking into account design constraints for achieving a stable system. Distinct solutions can be adopted for adjusting the required parameters, whereas this work has used conventional tuning techniques for this purpose.

When synthesizing the voltages $\vec{e}_{abc}$ defined in (40) using PWM, the synchronverter behaves as a conventional synchronous machine capable of injecting active power into the grid while considering the grid frequency as a control variable. Similarly, it can control the reactive power by controlling the grid voltage amplitude. The active and reactive power flowing through the synchronverter in Fig. 13 can be calculated from (48) and (49), respectively [36].

$$P = \frac{|E||V_g|}{X_s} \sin(\delta), \qquad (48)$$

$$Q = \frac{|V_g|}{X_s} \left[|E|\cos(\delta) - |V_g| \right], \qquad (49)$$

where E is the RMS value of the voltage synthesized by the synchronverter obtained from $\vec{e}_{abc}$, whose frequency and phase angle are $\dot{\theta}_v$ and θ_v, respectively; V_g is the RMS value of the grid voltage, whose frequency and phase angle are $\dot{\theta}_g$ and θ_g, respectively; X_s is the inductive reactance, considering that the resistance R_s is negligible; and $\delta = \theta_v - \theta_g$ is the load angle.

If $\delta > 0$ in (48), the synchronverter will supply active power to the grid, but absorb it instead if $\delta < 0$. Similarly, controlling the value of E in (49) allows injecting or absorbing reactive power. Thus, the active power control for frequency support relies on angle θ_v as demonstrated

in this work.

The authors in [37] and [38] propose a small-signal model for investigating the stability and dynamic interactions between the synchronverter control system and a power network. By modifying (41), which corresponds to the active power control loop in Fig. 13, as well as considering that the term associated with $D_p \dot{\theta}$ is analogous to the speed regulator without a time delay, one can obtain (50), which provides the frequency droop control.

$$J\ddot{\theta}_v = T_m - T_e - D_p(\dot{\theta}_v - \dot{\theta}_n). \qquad (50)$$

In turn, the reactive power control loop in Fig. 13 relies on the relationship between the active power and the grid voltage, also being responsible for providing the voltage droop control. Thus, one can represent (46) and (47) in terms of a general equation as in (51).

$$M_f i_f = \frac{1}{K} \left[(Q_{set} - Q) - D_q(v_n - v_{abc}) \right]. \qquad (51)$$

One can represent the linearized dynamics of the synchronverter from a state-space notation considering the vectors given in (52), (53) and (54).

$$\Delta x = \begin{bmatrix} \Delta M_f i_f \\ \Delta \dot{\theta}_v \\ \Delta \theta_v \end{bmatrix}, \qquad (52)$$

$$\Delta u = \begin{bmatrix} \Delta P_{set} \\ \Delta P \\ \Delta Q_{set} \\ \Delta Q \\ \Delta V_{abc} \end{bmatrix}, \qquad (53)$$

$$\Delta y = \begin{bmatrix} \Delta E_p \\ \Delta \theta_v \end{bmatrix}, \qquad (54)$$

where E is the amplitude of $\vec{e}_{abc}$ as calculated from $M_f i_f \dot{\theta}$ in (40).

The control system can then be represented in the form of state-space equations in (55).

$$\begin{cases} \Delta \dot{x} = A\Delta x + B\Delta u \\ \Delta y = C\Delta x + D\Delta u \end{cases}, \qquad (55)$$

where A, B, C, D are the state-space matrices.

Considering Fig. 13 and adding small-signal perturbations to (50) and (51), it is possible to obtain (56) and (57), respectively.

$$\Delta \ddot{\theta}_v = \frac{\Delta T_m}{J} - \frac{\Delta \dot{\theta}_v}{J} D_p - \frac{\Delta P}{J \dot{\theta}_v}. \qquad (56)$$

$$\Delta M_f i_f = \frac{\Delta Q_{set}}{K} - \frac{\Delta Q}{K} - \frac{\Delta V_{abc} D_q}{K}. \qquad (57)$$

Adding a small-signal perturbation to θ_v yields (58).

$$\Delta \dot{\theta}_v = \Delta \ddot{\theta}_v. \qquad (58)$$

One can also linearize E_p around the operating point defined by $M_f i_{f0}$ and $\dot{\theta}_{v0}$ according to (59).

$$\Delta E_p = M_f i_{f0} \Delta \dot{\theta}_v + M_f i_f \Delta \dot{\theta}_{v0}. \qquad (59)$$

The state-space matrices are defined in (60) – (63).

$$A = \begin{bmatrix} 0 & 0 & 0 \\ 0 & -\dfrac{D_p}{J} & 0 \\ 0 & 1 & 0 \end{bmatrix}, \qquad (60)$$

Table 5
Parameters of the synchronverter-based GSC control.

Grid	Value
Rated grid line voltage (V_g, V_n)	0.69 kV
Rated frequency (f)	60 Hz
Synchronverter	Value
Filter inductance (L_s)	1.7 mH
Filter resistance (R_s)	0.01 Ω
Filter capacitance (C)	300 µF
Dc-link capacitance (C_{dc})	100 mF
Frequency droop coefficient (D_p)	50 kW/Hz
Voltage droop coefficient (D_q)	5 kvar/V
Time constant of the frequency loop (τ_f)	2 ms
Time constant of the voltage loop (τ_v)	50 ms
Dc-link voltage (V_{dc})	2.5 kV
Proportional and integral constants of the PI controller (k_p, T_i)	0.82, 0.1 s

$$B = \begin{bmatrix} 0 & 0 & \dfrac{1}{K} & -\dfrac{1}{K} & -\dfrac{D_q}{K} \\ \dfrac{1}{J\dot\theta_{v0}} & -\dfrac{1}{J\dot\theta_{v0}} & 0 & 0 & 0 \\ 0 & 0 & 0 & 0 & 0 \end{bmatrix}, \tag{61}$$

$$C = \begin{bmatrix} \dot\theta_{v0} & M_f i_{f0} & 0 \\ 0 & 0 & 1 \end{bmatrix}, \tag{62}$$

$$D = [0]_{2\times5}, \tag{63}$$

The behavior of the state-space model of the synchronverter was thoroughly assessed in [38] in MATLAB/Simulink environment. The results did demonstrate that it can represent the dynamic behavior of the system accurately by adjusting the frequency droop coefficient D_p, the voltage droop coefficient D_q, the virtual inertia J, and the integrator gain K. Given the above, it is possible to obtain the parameters of the synchronverter-based control system of the GSC in Table 5.

4. Results and discussion

To assess the performance of pitch angle control and SAC and compare them with the introduced approach, this section presents some case studies on the 14-bus IEEE modified test system. As previously mentioned, it comprises a 165 MW WF composed of 33 5 MW DFIGs connected to bus #1. This WF is supposed to replace two synchronous generators that were formerly connected to the same bus, thus keeping the total system power constant at 412.5 MW. The active power output of the WF is reduced by the controller using the de-loading approach, with the increase of the pitch angle to 2° when the system frequency is at the rated value of 60 Hz. Thus, it causes the active power of the WF to be 137 MW, corresponding to a reduction of 16.8% in the maximum value. In this case, the exceeding power is supplied by the synchronous generators to maintain the total power constant. When using the synchronverter, the energy required to provide frequency control is supplied by the battery bank, whereas it is not necessary to reduce the power output of the WF. In other words, the pitch angle remains at 0° and the WF operates at 165 MW.

It is assumed that the dynamic behavior of the system frequency complies with the frequency requirements of the Brazilian national interconnected system defined in [39]. In a steady-state condition, WFs should remain connected to the grid when subjected to frequencies between 58.5 Hz and 62.5 Hz. Between 58.5 Hz and 56.0 Hz, they must operate during a minimum time interval of 20 s. Between 62.5 Hz and 63.0 Hz, they must operate during a minimum time interval of 10 s. The disconnection can be instantaneous outside the aforementioned ranges.

The 165-MW WF can supply up to 39.7% of the total system load for the rated condition, representing three times the penetration percentage of all wind and photovoltaic plants of the Brazilian national interconnected system, which is currently equivalent to 12.28% [39]. The
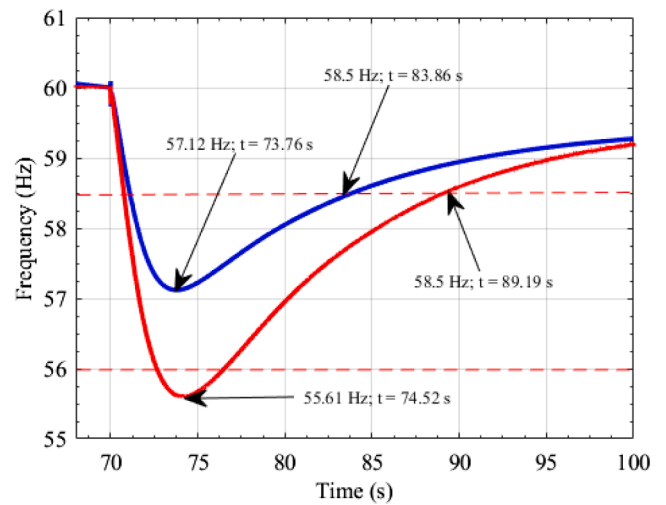

Fig. 14. Frequency variation with (red) and without (blue) the WF and no frequency control.

WF operates with a constant wind speed $V_w = 11$ m/s. A load rated at 60 MW/12 MVar is connected to bus #5 at $t = 70$ s after the starting transient of the 14-bus IEEE modified test system finishes and the system frequency is at 60.0 Hz. Simulation results of the DFIG without any frequency controller are denoted by "original", whereas the ones obtained with a frequency control approach are denoted by "pitch control", "SAC", or "synchronverter" in the plots. The SAC is enabled when the frequency deviation is ±0.15 Hz or higher. The power output of the SAC is analyzed considering $\Delta\delta = 0.3$ rad. In turn, the battery bank is connected to the dc link when the frequency drops below 59.5 Hz to allow active power injection from the synchronverter.

Fig. 14 shows that the frequency drops owing to the sudden load change, becoming as low as 55.61 Hz at $t = 74.52$ s when no frequency control approach is used. Under these conditions, the WF does not provide frequency support, leading to the system disconnection due to underfrequency. Considering a power system composed of synchronous machines only and without the WF, the frequency oscillation would be lower, with a minimum of 57.12 Hz at $t = 73.76$ s. In other words, considering a scenario in which no WFs remain connected to the system, but only synchronous generators, such a load step would not cause the violation of the minimum threshold of 56 Hz and system shutdown. Furthermore, the time interval during which the frequency is below 58.5 Hz in the presence of WF would be longer and equal to 18.43 s,
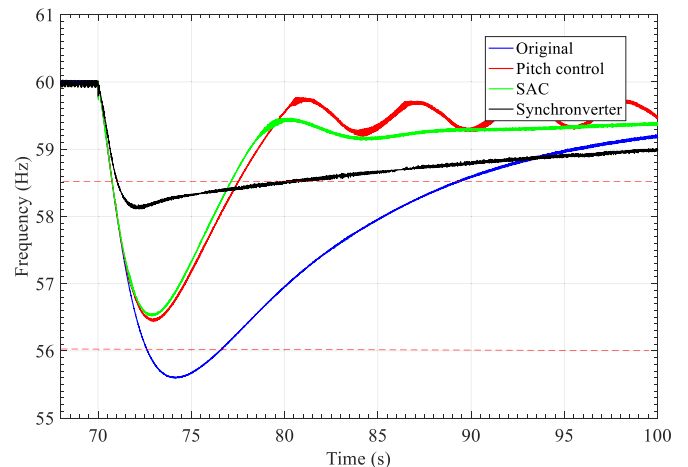

Fig. 15. Frequency variation without frequency control (blue) and using pitch control (red), SAC (green), and the synchronverter (black).
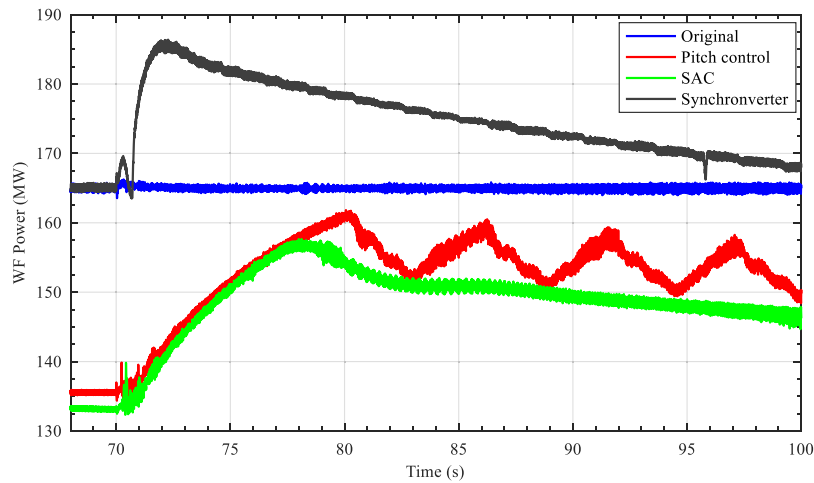
Fig. 16. WF power output without frequency control (blue) and using pitch control (red), SAC (green), and the synchronverter (black).

instead of 13.1 s when only synchronous generators exist.

After incorporating the pitch control and SAC into the system, it is observed that the SAC results in a lower frequency deviation according to Fig. 15. The frequency oscillates up to 56.52 Hz during a time interval of 6.34 s, corresponding to a drop of 5.8% in the rated value. In turn, the frequency becomes as low as 56.44 Hz and returns to 58.5 Hz in 6.74 s when the pitch control is used, representing a reduction of 5.93%. Thus, the minimum frequency is 2.2% higher and the required time interval to achieve 58.5 Hz is 5.9% shorter when using SAC. When the synchronverter is used, the system performance during the frequency support is significantly enhanced. Fig. 15 shows that the frequency drops to 58.11 Hz and returns to 58.5 Hz in 9.04 s, corresponding to a drop of 3.15%.

Fig. 16 presents the DFIG response in the four scenarios, where the SAC provides a lower reference power output than the pitch control, but with a slightly improved performance. The greater power variation in pitch control is because the strategy adopts binary values for angle β, that is, $2°$ or $0°$. The synchronverter is capable of providing an additional power of 20 MW without the need for reducing the power output of the WF owing to the battery bank. The fast dynamic response of the
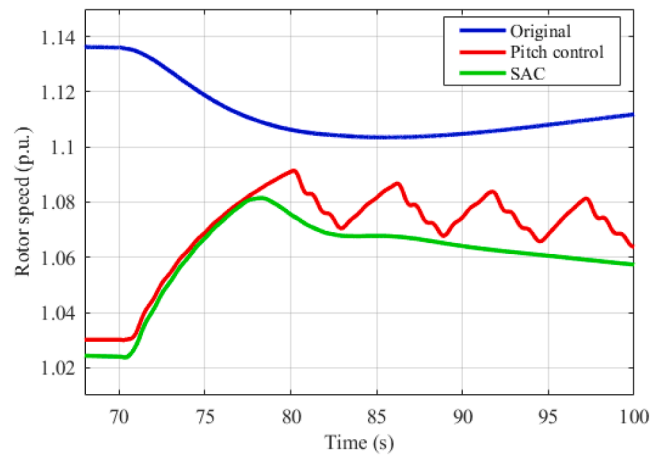

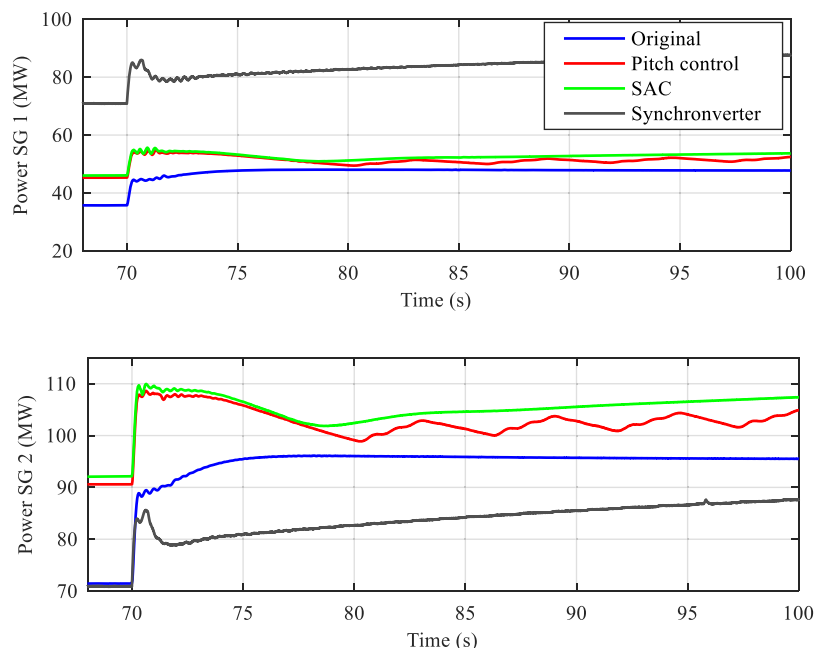
Fig. 18. Rotor speed of the DFIG.

Fig. 17. Active power of the synchronous generators connected to buses #2 and #5.
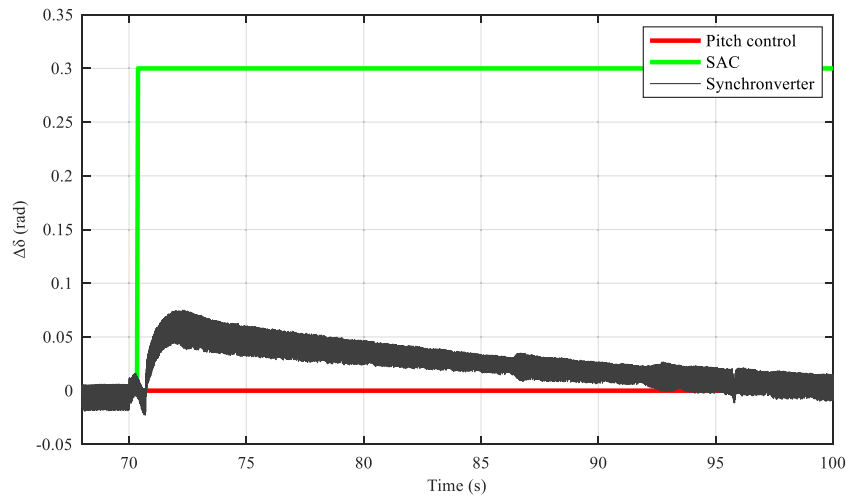
Fig. 19. Behavior of the pitch angle (red) and virtual angles of SAC (green) and synchronverter (black).

proposed solution also contributes to the lower frequency deviation, especially when compared with SAC and pitch angle control. Fig. 17 shows the power variation of the synchronous generators in response to changes in the WF power generation.

It is also verified that the DFIG rotor speed varies according to its active power output. Fig. 18 evidences that the rotor decelerates to release kinetic energy when an additional amount of active power is supplied by the WF at $t = 70$ s. When the system frequency is close to the rated value, the rotor accelerates again to store more kinetic energy. The rotor speed does not vary in the synchronverter control, which does not rely on de-loading. Fig. 19 also shows that the virtual angle of the SAC changes to 0.3 rad at $t = 70$ s. The virtual angle of the synchronverter represented by θ_v varies according to (41).

Despite the frequency variation decreasing when the pitch control and SAC are used in Figs. 14 and 15, respectively, it is reasonable to state that the values assumed by this parameter are still higher when compared with the case in which the WF does not exist in the test system. This issue confirms the loss of system inertia with the penetration of inverter-based generation units such as WFs with frequency support based on de-loading. In turn, it is not necessary to reduce the power output when using the synchronverter, whereas the frequency dip is smaller when there are only synchronous generators. Considering that such rotating machines are essential for maintaining the system stability, WFs based on synchronverters can emulate this behavior and supply active power with a faster dynamic response.

Table 6
Comparison among the frequency control strategies.

Parameter	Original	Pitch control	SAC	Synchronverter-based control
Nadir frequency (Hz)	55.61	56.44	56.52	58.11
Time interval required to achieve the nadir frequency (s)	74.52	72.85	73.03	72.5
RoCoF (Hz/s)	1.88	1.82	1.8	1.18
Time interval during which the frequency is below 58.5 Hz (s)	18.43	6.74	6.34	9.04
Maximum power in steady-state condition (MW)	165	133	133	165
Maximum power supplied during the frequency dip (MW)	165	160	156	185
Time interval required to achieve the maximum power (s)	*	10.25	7.85	1.96

Table 6 summarizes the results obtained so far while comparing the proposed technique with the WECS without frequency support, as well as employing pitch control and SAC when a load step of 60 MW/12 Mvar occurs at $t = 70$ s. It is worth mentioning that the minimum frequency is also referred to as the nadir frequency, which should be as high as possible during the dip. It is observed that the synchronverter-based control achieves the highest value of the nadir frequency while requiring the shortest time interval among the assessed approaches. It is still capable of maximizing the power supply during the frequency dip owing to the battery bank.

5. Conclusion

This work has presented a dynamic model of the 14-bus IEEE test system by including synchronous generators, whose parameters were obtained from a real power plant. The adoption of test systems using parameters of real synchronous generators provides the results with more reliability, also allowing a better understanding of distinct phenomena that occur in power systems, which include voltage transients and frequency variation. This is because the response of generators to short-circuit events or load changes does not only depend on the inertia of the system, but also the machine characteristics in terms of the moment of inertia, adjustment and characteristics of the exciter, control, and robustness of the system, as well as the operating point.

The short-circuit levels of specific bars were calculated and the results could be validated when the system was submitted to a frequency oscillation event during a sudden load increase. After validation, the model was used to verify the behavior of a power system comprising a 165 MW DFIG-based WF, corresponding to 39.7% of the overall generation. The impact of the WF on the frequency variation was assessed when a load of 60 MW/12 Mvar was added to bus #5.

A novel synchronverter-based frequency support solution was introduced, in which the GSC emulates the behavior of a synchronous generator and supplies active power based on the swing equation. A battery bank connected in parallel with the dc link is responsible for providing the required amount of energy. This solution was thoroughly compared with two classical de-loading strategies: pitch angle control and SAC. When the WF is incorporated into the system without any frequency control support, the frequency dropped to 55.61 Hz with an additional loading of 60 MW/12 Mvar, returning to the minimum threshold of 58.5 Hz in 19.9 s. Of course, this would trigger the protection system in practice. Thus, it becomes evident that the higher penetration of renewable energy sources without frequency support may lead to loss of inertia.

After the incorporation of the primary frequency control techniques,

it is observed that the frequency deviation is lower, resulting in a shorter recovery time. Thus, the synchronverter outperformed SAC, which in turn performed slightly better than pitch angle control. This is due to the higher power output provided by the synchronverter when compared with the scenario in which the WF is not included. Overall, it is reasonable to state the IEEE 14-bus modified test system can be used for the assessment of other frequency control techniques than the ones investigated in this work. This aspect is of major interest not only to compare the existing approaches but also to contribute to the development of new strategies.

Data availability statement

Data available on request from the authors.

CRediT authorship contribution statement

José Dickson Araújo de Oliveira: Methodology, Validation, Investigation. **Francisco Kleber de Araújo Lima:** Conceptualization, Supervision. **Fernando Lessa Tofoli:** Writing – original draft, Writing – review & editing. **Carlos Gustavo Castelo Branco:** Validation, Investigation.

Declaration of Competing Interest

The authors declare that they have no known competing financial interests or personal relationships that could have appeared to influence the work reported in this paper.

Data Availability

Data will be made available on request.

References

[1] R. Akbari, A. Izadian, R.S. Weissbach, Quasi self-excited dfig-based wind energy conversion system, IEEE Trans. Ind. Appl. 57 (3) (2021) 2816–2824.
[2] H.H. Mousa, A.-.R. Youssef, E.E. Mohamed, State of the art perturb and observe MPPT algorithms based wind energy conversion systems: a technology review, Int. J. Electrical Power Energy Syst. 126 (2021), 106598.
[3] X. Zhao, Z. Lin, B. Fu, S. Gong, Research on frequency control method for micro-grid with a hybrid approach of FFR-OPPT and pitch angle of wind turbine, Int. J. Electrical Power Energy Syst. 127 (2021), 106670.
[4] M. Debouza, A. Al-Durra, Grid ancillary services from doubly fed induction generator-based wind energy conversion system: a review, IEEE Access 7 (2019) 7067–7081.
[5] A. Radaideh, A. Al-Quraan, H. Al-Masri, Z. Albataineh, Rolling horizon control architecture for distributed agents of thermostatically controlled loads enabling long-term grid-level ancillary services, Int. J. Electrical Power Energy Syst. 127 (2021), 106630.
[6] J.X. Jin, R.H. Yang, R.T. Zhang, Y.J. Fan, Q. Xie, X.Y. Chen, Combined low voltage ride through and power smoothing control for DFIG/PMSG hybrid wind energy conversion system employing a SMES-based AC-DC unified power quality conditioner, Int. J. Electrical Power Energy Syst. 128 (2021), 106733.
[7] B.B. Adetokun, C.M. Muriithi, Impact of integrating large-scale DFIG-based wind energy conversion system on the voltage stability of weak national grids: a case study of the Nigerian power grid, Energy Rep. 7 (2021) 654–666.
[8] Y.L. Hu, Y.K. Wu, Inertial response identification algorithm for the development of dynamic equivalent model of DFIG-based wind power plant, IEEE Trans. Ind. Appl. 57 (3) (2021) 2104–2113.
[9] X. Yingcheng, T. Nengling, Review of contribution to frequency control through variable speed wind turbine, Renew. Energy 36 (6) (2011) 1671–1677.
[10] N.R. Ullah, T. Thiringer, D. Karlsson, Temporary primary frequency control support by variable speed wind turbines—potential and applications, IEEE Trans. Power Syst. 23 (2) (2008) 601–612.
[11] A. Molina-García, I. Muñoz-Benavente, A.D. Hansen, E. Gómez-Lázaro, Demand-side contribution to primary frequency control with wind farm auxiliary control, IEEE Trans. Power Syst. 29 (5) (2014) 2391–2399.
[12] B. Liu, J. Zhao, Q. Huang, F. Milano, Y. Zhang, W. Hu, Nonlinear virtual inertia control of WTGs for enhancing primary frequency response and suppressing drivetrain torsional oscillations, IEEE Trans. Power Syst. 36 (5) (2021) 4102–4113.
[13] Q.-.C. Zhong, G. Weiss, Synchronverters: inverters that mimic synchronous generators, IEEE Trans. Ind. Electron. 58 (4) (2011) 1259–1267.
[14] G.P. da Silva Junior, L.S. Barros, C.M.V. Barros, Synchronverter coupled to a lithium-ion bank for grid frequency and voltage supports and controlled charge-discharge, Electric Power Syst. Res. 197 (2021), 107352.
[15] A.J. Sonawane, A.C. Umarikar, Small-signal stability analysis of PV-based synchronverter including PV operating modes and DC-link voltage controller, IEEE Trans. Ind. Electron. 69 (8) (2022) 8028–8039.
[16] R. Hariharan, M.K. Mishra, An improved synchronverter control for DERs under grid voltage variations, in: 2021 IEEE 2nd International Conference on Smart Technologies for Power, Energy and Control (STPEC), 2021, pp. 1–6.
[17] M. Garmroodi, G. Verbič, D.J. Hill, Frequency support from wind turbine generators with a time-variable droop characteristic, IEEE Trans. Sustain. Energy 9 (2) (2018) 676–684.
[18] Y. Liu, L. Jiang, Q.H. Wu, X. Zhou, Frequency control of DFIG-based wind power penetrated power systems using switching angle controller and AGC, IEEE Trans. Power Syst. 32 (2) (2017) 1553–1567.
[19] H. Geng, X. Xi, L. Liu, G. Yang, J. Ma, Hybrid modulated active damping control for DFIG-based wind farm participating in frequency response, IEEE Trans. Energy Convers. 32 (3) (2017) 1220–1230.
[20] X. Liu, Y. Zhang, K.Y. Lee, Coordinated distributed MPC for load frequency control of power system with wind farms, IEEE Trans. Ind. Electron. 64 (6) (2017) 5140–5150.
[21] H. Ali, G. Magdy, B. Li, G. Shabib, A.A. Elbaset, D. Xu, et al., A new frequency control strategy in an islanded microgrid using virtual inertia control-based coefficient diagram method, IEEE Access 7 (2019) 16979–16990, no.
[22] (May 2018). Manitoba Hydro International Ltd., IEEE 14 Bus System. Winnipeg, Manitoba, Canadá. Available: https://www.pscad.com/knowledge-base/download/ieee_14_bus_technical_note.pdf.
[23] (October 2018). Report PE-DEE-RE-097/2007-r1 - AHE Santo Antônio – Technical Viability Study – Project Optimization. Brasília, DF, Brazil. . Available: https://www.epe.gov.br/sites-pt/publicacoes-dados-abertos/publicacoes/PublicacoesArquivos/publicacao-84/EPE-DEE-RE-097-2007-r1.pdf.
[24] P. Demetriou, M. Asprou, J. Quiros-Tortos, E. Kyriakides, Dynamic IEEE test systems for transient analysis, IEEE Syst. J. 11 (4) (2017) 2108–2117.
[25] (September 2021). Illinois center for a smarter electric grid (ICSEG). Available: https://icseg.iti.illinois.edu/.
[26] O. Anaya-Lara, N. Jenkins, J.B. Ekanayake, P. Cartwright, M. Hughes, Wind Energy Generation: Modelling and Control, John Wiley & Sons, 2011.
[27] J.J. Grainger, Power System Analysis, McGraw-Hill, 1999.
[28] (September 2021). ENTSO-E SPD WG - Inertia and Rate of Change of Frequency (RoCoF). Brussels, Belgium. Available: https://eepublicdownloads.entsoe.eu/clean-documents/Network%20codes%20documents/NC%20RfG/IGD_RoCoF_withstand_capability_final.pdf.
[29] F.K.A. Lima, A. Luna, P. Rodriguez, E.H. Watanabe, F. Blaabjerg, Rotor voltage dynamics in the doubly fed induction generator during grid faults, IEEE Trans. Power Electron. 25 (1) (2010) 118–130.
[30] A. Zertek, G. Verbic, M. Pantos, A novel strategy for variable-speed wind turbines' participation in primary frequency control, IEEE Trans. Sustain. Energy 3 (4) (2012) 791–799.
[31] P. Bousseau, R. Belhomme, E. Monnot, N. Laverdure, D. Boëda, D. Roye, et al., Contribution of wind farms to ancillary services, Cigre 21 (2006) 1–11.
[32] L. Ruttledge, D. Flynn, Emulated inertial response from wind turbines: gain scheduling and resource coordination, IEEE Trans. Power Syst. 31 (5) (2016) 3747–3755.
[33] T. Wang, L. Ding, S. Yin, J. Jiang, F. Cheng, J. Si, A new control strategy of DFIG-based wind farms for power system frequency regulation, in: 2015 IEEE PES Asia-Pacific Power and Energy Engineering Conference (APPEEC), 2015, pp. 1–5.
[34] P. Kundur, Power System Stability, McGraw-Hill Professional Publishing, 2006.
[35] Q.-.C. Zhong, Power Electronics-Enabled Autonomous Power Systems: Next Generation Smart Grids, John Wiley & Sons, 2020.
[36] W. Stevenson Jr, J. Grainger, Power System Analysis, McGraw-Hill Education, 1994.
[37] K.R. Vasudevan, V.K. Ramachandaramurthy, T.S. Babu, A. Pouryekta, Synchronverter: a comprehensive review of modifications, stability assessment, applications and future perspectives, IEEE Access 8 (2020) 131565–131589.
[38] R. Rosso, J. Cassoli, G. Buticchi, S. Engelken, M. Liserre, Robust stability analysis of LCL filter based synchronverter under different grid conditions, IEEE Trans. Power Electron. 34 (6) (2019) 5842–5853.
[39] (September 2021). Sistema de Informações de Geração da ANEEL - SIGA. Brasília, DF, Brasil. Available: https://www.aneel.gov.br/siga.